Bonding and microstructure evolution in electromagnetic pulse welding of hardenable Al alloys

Z. Li[a], E. Beslin[b], A. J. den Bakker[b], G. Scamans[a,c], M. Danaie[d], C. A. Williams[c], and H. Assadi[a*]

[a]Brunel Centre for Advanced Solidification Technology (BCAST), Brunel University London, UK

[b]Constellium University Technology Centre, Brunel University London, UK

[c]Innoval Technology Ltd, Banbury, UK

[d]Electron Physical Sciences Imaging Centre (ePSIC), Diamond Light Source, Oxford, UK

Abstract

Electromagnetic pulse welding (EMPW) is a promising solid-state joining process, offering fast and strong bonding with no heat affected zone. Despite the growing interest in this process, there is little understanding of the dynamic phenomena that lead to bonding and microstructural changes during EMPW of key engineering materials such as age-hardenable aluminium alloys. This study combines experiments with numerical modelling of plastic deformation to provide an insight to these phenomena in joining of a high-strength aluminium alloy in the T4 and T6 temper conditions. Initially, bonding criteria are postulated in view of the calculated plastic strain at the interface of the T4 sample. These criteria are then used for the prediction of the extent of bonded interfaces for different sets of materials and process parameters. The predictions are shown to be in quantitative agreement with the experimental

---

[*] Corresponding author. *E-mail address:* hamid.assadi@brunel.ac.uk (H. Assadi).

results for the T6 sample. The corresponding microstructural studies show that bonding is associated with remarkable microstructural changes in the samples, including dissolution of precipitates, formation of high-angle boundaries, and recrystallisation, especially near the bonded interfaces. Moreover, the results of post-weld heat treatments and mechanical testing demonstrate that the impact-induced deformation in EMPW can also influence subsequent precipitations, hence result in improved properties of the entire sample, in a way not achievable by conventional age hardening treatments.

Keywords: Electromagnetic pulse welding, Bonding, Finite element analysis, Microstructure, Aluminium alloys.

1. Introduction

Electromagnetic pulse welding (EMPW) is a fast and reliable joining process, which is becoming increasingly attractive for various industrial applications, particularly in manufacturing with high-strength aluminium alloys. In this process, a high-energy magnetic field is used to accelerate a flyer workpiece towards a (similar or dissimilar) substrate, leading to a high-velocity impact and solid-state bonding, without forming a detrimental heat affected zone (HAZ). Kore et al. (2011), Bellmann et al. (2016), Shanthala and Sreenivasa (2016), and Pereira et al. (2018) provide descriptions of the EMPW process and its applications. Many studies, including those by Kwee et al. (2016) and Shribman (2008), suggest that the high-velocity impact leads to the removal of oxides and contamination from the interacting surfaces, hence to the formation of an atomic bond between the two metal workpieces. Palmer et al. (2006) reported that the impact could also be associated with mechanical intermixing, severe plastic deformation and localized melting/re-solidification. Moreover, formation of a jet between the surfaces during joining has been considered as an important prerequisite for successful welding. Kapil and Sharma (2015) describe jet formation as a mechanism to clean the surface from contamination and oxides, while the impact forces continue to press the metal plates together enabling a metallurgical bond.

Interface morphology: EMPW can also be associated with the formation of a wavy interface. This feature has prompted several researchers to focus on the interface morphology of the EMPW joints. Nassiri et al. (2014) described a wavy interface as the outcome of a 'shear instability' – which should be distinguished from the adiabatic shear instability (ASI) as referred to later in this paper. Ben-Artzy et al. (2010) attributed this morphological instability to a Kelvin–Helmholtz instability mechanism. Psyk et al. (2011) and Elsen et al. (2010) reported that the formation of a wavy interface depended on the velocity of impact, while Shribman (2007) suggested that material properties also could play a role. However, the

literature is not conclusive on the role of interface morphology in bonding. Göbel et al. (2010) and Groche et al. (2014) posited that a wavy interface was not necessary to obtain a successful weld. Parchuri et al. (2019) suggested that a wavy interface could improve the joint strength because of mechanical interlocking, whereas Acarer et al. (2003) reported no obvious difference in strength between wavy and flat interfaces.

Local melting: There has also been some debate in the literature on the likelihood and the role of melting and re-solidification in EMPW. Göbel et al. (2010) and Ben-Artzy et al. (2008) considered the presence of an intermetallic phase at the interface as an indication of interfacial melting in joining of dissimilar metals. Raoelison et al. (2015) suggested the formation of an amorphous phase at the interface resulted from localised melting followed by rapid solidification. Nassiri et al. (2015) used numerical simulations to show that interfacial melting could occur in EMPW of Al6061-T6 workpieces when the impact velocity was higher than 500 m/s. In a more recent study of EMPW of dissimilar metals (Cu/Al6060-T6), Li et al. (2020) provide conclusive evidence, backed by numerical analysis, for interfacial melting under extremely severe impact conditions, i.e. with impact velocities in the range 600-900 m/s. Although there is little published literature on the EPMW of similar metals, it is conceivable that melting can also occur during joining of similar metals at extremely high impact velocities. However, Kapil and Sharma (2015) argued that for typical EMPW conditions, the increase of temperature at the interface was often not high enough to melt any of the mating members. Also, Uhlmann and Ziefle (2010) reported that melting could always be avoided by either decreasing the energy level or by changing the impact angle. Although there is evidence that melting can occur under certain conditions, there is no consensus about the necessity of local melting to achieve a strong weld. Since melting and re-solidification can lead to the formation of solidification defects and brittle intermetallic phases, it is reasonable to assume that melting is generally unfavourable for bonding. In any case, the most relevant

questions – in addition to whether or under what conditions melting can occur – are: (1) whether melting is essentially a favourable feature, and (2) whether melting is a prerequisite for bonding, i.e. it can play a decisive role in joint formation.

Microstructure: Further to the questions of interface morphology, melting, and their roles in bonding, Lee et al. (2020) and Chen et al. (2016) provide an extensive discussion of the microstructure of the EMPW joints. Nevertheless, the effect of EMPW on different aspects of microstructure evolution – e.g. in terms of grain structure or distribution of precipitates, which are central to the mechanical strength of age-hardenable aluminium alloys – is yet to be fully understood.

Objectives: The aim of the current study is twofold: (1) to shed light on the bonding mechanism at the micro-level in EMPW, by focusing on the interfacial conditions that are deemed to be relevant to bonding, and (2) to devise a quantitative bonding criterion that can be used as a basis for process optimisation, for any given set of materials properties.

Bonding mechanism: To provide a new angle on the bonding mechanism in EMPW, the dynamic phenomena in this process may be compared to those in explosive welding and cold spraying (CS). In all these processes, bonding results from high-velocity impact and the associated high-strain rate deformation. Specifically, there is a characteristic critical velocity for bonding in all these processes, relating to the speed of plastic wave in the material. Exceeding this characteristic velocity is often manifested by material jetting, which is a key feature in all these processes. For instance, Hammerschmidt and Kreye (1981) and McCune et al. (1995) demonstrated – in explosive welding and CS, respectively – that the generated high-velocity impact is associated with localised deformation and manifested by material jetting from the colliding surfaces. These similarities clearly encourage transfer of the existing experience in explosive welding and CS to EMPW, e.g. with regards to the influence of material properties on the critical velocity, despite differences in the length scale. It should be

noted that the size of objects in impact-induced bonding is of a lesser significance, so that the principles of bonding mechanisms should be somewhat transferable across different length scales, Assadi et al. (2016). For example, a common key principle is that bonding is closely linked to the development of high plastic strains at the interface. In this study, we follow the same principle and focus on the evolution of interfacial strains.

Bonding criterion: A central challenge in the application of EMPW is to identify and optimise the conditions that lead to successful bonding. In analogy with explosive welding, Nassiri et al. (2019) posit that successful joining takes place when the impact angle (α) and the impact velocity (v_i) fall within a certain range. Zhang et al. (2010) report that the impact velocity for successful bonding is typically in the range 200-400 m/s. It is conceivable that the range of impact of velocity for successful bonding (i.e. the 'bonding window') is not an invariant and that it should depend on material properties. For instance, Weddeling et al. (2012) show that hardness is a key factor in EMPW. Despite these findings, a comprehensive correlation between material properties and the bonding window is yet to be established. Even if the bonding window is known, a remaining challenge will be to achieve the desired values of α and v_i, which cannot be set directly on the equipment. Kwee et al., (2016) and Raoelison et al. (2013) show that both α and v_i depend on several primary process parameters, such as workpiece dimensions, airgap, overlap and charge energy from the welding setup. Also, the physical properties of the material (including density and electromagnetic properties) will have a major influence on the acceleration of the flyer workpiece, and hence on the impact velocity. Thus, contriving a general bonding criterion and subsequently optimising the EMPW process with respect to α and v_i is not straightforward. There is yet another complication: In contrast to explosive welding, α and v_i in EMPW are often not constant. This is mainly due to the inhomogeneous distribution of the electromagnetic forces, which are localised to a small region around the coil.

The challenge: Understanding the bonding mechanism and devising a bonding criterion require a detailed analysis of the dynamic phenomena at the interface. However, the very short process time (commonly less than100 µs in EMPW), besides the opacity of the materials, makes it almost impossible to perform direct experimental observation of the dynamic interaction of the contact surfaces and to investigate the bonding mechanism at the micro-level. To address this problem, modelling and simulation of the process can be used to gain a better insight into the relevant dynamic phenomena at the interface. There have been several studies of EMPW using this technique, including those by Bellmann et al. (2016) Bataev et al. (2019), and Li et al. (2020).

Our approach: In this paper, we aim to combine experiments with numerical modelling to provide a detailed analysis of the dynamic phenomena responsible for bonding. Numerical simulations of the impact are performed in order to gain an insight to the development of thermomechanical field variables within the material, particularly at and around the interface. Based on this, a bonding criterion is devised, which can provide guidelines for parameter selection at the process level. The proposed criterion is also used to predict the extent of bonding for various material properties and process conditions. Moreover, we investigate the impact of EMPW on the microstructure, particularly in relation to the effect of high strain-rate deformation on the evolution of grain structure and precipitates under different processing conditions.

2. Methods

2.1. Materials and processing

To investigate the impact of EMPW on the microstructure, especially with regards to precipitation, a Constellium's patented commercial high-strength 6000-series aluminium extrusion alloy (Constellium HSA6^{TM}) was welded in both the T4 (solution heat treatment,

naturally aged) and T6 (heat-treated to maximum strength) temper conditions. Both joints were also subjected to a post-joining ageing practice (comparable to the T6 ageing practice) for further microstructural studies. Sections of a 2 mm thick extrusion were machined to a width of 200 mm. Their hardness and tensile properties are shown in Table 1.

Table 1. Tensile properties of the examined aluminium samples

Temper	Hardness [HV]	Yield strength $(R_{p0.2})$ [MPa]	Tensile strength (R_m) [MPa]	Elongation [%]
T4	84±2	191±5	305±7	21±1.8
T6	112±2	315±2	351±3	9±0.4

A pulsed power generator PS96-16 Blue Wave with a maximum capacitor charging energy and voltage of 96 kJ and 16 kV, respectively, from PSTproducts GmbH was used in this work. Figure 1 shows a schematic cross-sectional view of the EMPW setup. The flyer workpiece sits 2 mm away from the target, with an 8 mm overlap. A discharge energy of 50 kJ was used, which produced a primary current pulse approximating a damped sine wave with a peak amplitude of 655 kA and a frequency of 17.37 kHz through the coil.
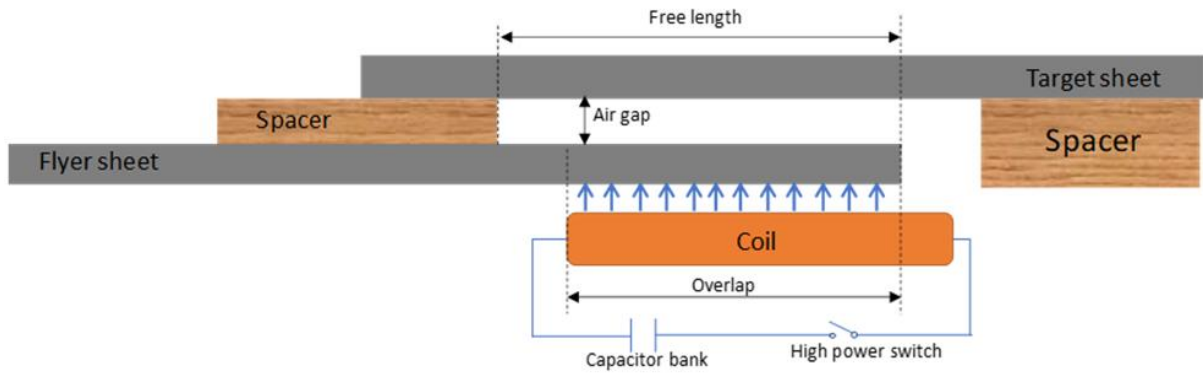
Figure 1. Schematics of the active section of the EMPW setup.

2.2. Characterisation methods

After welding, the joints were broken open mechanically to examine the weld quality. Raoelison et al. (2013) provide a description of this method. For the successfully welded samples, the central parts containing the longest weld interface were cross-sectioned and prepared for metallographic examination by optical microscopy. The changes in mechanical properties of the joint area were inferred from a hardness profile across the joint in the longitudinal and transverse directions. These profiles were generated using a Vickers hardness indenter operating under 100 gf / 12s as per BS EN ISO 6507-1.

Electron backscatter diffraction (EBSD) was carried out using a Zeiss Supra 35VP scanning electron microscope operating at 20 kV. The surface preparation for EBSD samples was conducted by standard metallographic grinding and polishing steps followed by vibration polishing for 3 h on a 0.05-μm colloidal silica suspension using a VibroMet 2 apparatus from Buehler. The EBSD scanning step sizes were 0.25 and 0.5 μm for the welded and base material regions, respectively. The obtained EBSD data were analysed by using TSL OIM Analysis software.

The microstructure was also examined by transmission electron microscopy (TEM). TEM samples were taken from two locations (reference and joint) and prepared by using precision

grinding holders to grind 3-mm discs to 100 μm thickness in the same plane as the surface of the flyer plate. The discs were then electropolished using a TenuPol electrolytic preparation equipment from Struers Ltd. with a solution of 25% nitric acid in methanol operating at -40 to -35 °C. Diffraction contrast TEM analysis was carried out in bright-field mode using a JEOL 2100 microscope with the sample orientated to the [001] zone axis. Atomic resolution imaging of the precipitates along the same zone axis was performed on a JEOL JEM-ARM 300F, equipped with spherical aberration corrector optics both in image and probe-forming modes, operated at 200 kV accelerating voltage. Annular dark-field (ADF) scanning transmission electron microscopy (STEM) images were acquired using a probe with 28.8 mrad convergence semi-angle, summing the scattered electrons intensity in the range of 79 to 240 mrad (9 cm camera length) to form an ADF image.

2.3. Modelling of deformation

The thermomechanical part of the EMPW process, including the acceleration, impact and viscoplastic deformation of the specimens, was simulated by using the dynamic temperature-displacement algorithm available in the finite element software, ABAQUS. The simulations were performed initially for the T4 sample, assuming a Johnson-Cook plasticity model for the flow stress with strain-rate sensitivity:

$$\sigma = (A + B\varepsilon^n)(1 + C \ln \dot{\varepsilon}^*)(1 - T^{*m}) \tag{1}$$

where σ is the flow stress, ε is the plastic strain, $\dot{\varepsilon}^*$ is the plastic strain rate normalised with respect to a reference strain rate (assumed here to be unity), and $T^* = (T-T_{ref})/(T_m-T_{ref})$ in which T_{ref} is the reference temperature (assumed here to be 25 °C), and T_m is the melting (solidus) temperature of the alloy. The constants A, B and n are chosen in a way as to correspond to the mechanical properties given in Table 1 – e.g. to give the same ultimate tensile strength, R_m, as obtained from the condition $d\sigma = d\sigma/d\varepsilon$. The Johnson-Cook and other

material parameters used for the simulations are given in Table 2. Simulations were performed for the T4 specimen in a 2D plane-strain domain, initially for a case with a 2-mm airgap between the target and the flyer plates.

A Lagrangian finite element method was used with distortion control and a minimum element size of 10-100 μm around the contact zone. The elements were 4-node plane strain thermally coupled quadrilateral, nonlinear displacement and temperature, reduced integration, with hourglass control. An inelastic heat fraction of 0.9 was considered to account for plastic dissipation. Linear elasticity was used predominantly throughout the study, while an equation of state (EOS) was considered to check the influence of thermoelastic heating under compression. The model did not include calculation of the electromagnetic forces and heat generation due to eddy current. The Lagrangian method was used to enable tracking the interface and applying customised interaction properties to the interface (in this case comprising a coefficient of friction of 0.5 and equal frictional dissipation to the master and slave surfaces). Moreover, the Lagrangian method was found to better resolve strain localisation as compared to arbitrary Lagrangian-Eulerian (ALE), which tend to smear out steep strain gradients. On the other hand, the Lagrangian method may suffer from excessive mesh distortion and so not suited for quantitative modelling of the interface morphology. To simulate morphological instabilities, Eulerian FEM, or smoothed particle hydrodynamics (SPH) would be more appropriate. However, for the purpose of the present study, which focuses on strain localisation at the surface, these methods do not offer a merit over Lagrangian FEM.

The loading due to the generated Lorenz force was mimicked by applying a non-uniform transient surface pressure on the flyer plate. The pressure amplitude was assumed to vary with time according to a half-sinusoidal relation over 30 μs, consistent with the measured frequency of about 17 kHz. The shape and the amplitude of the peak pressure was varied by

trial and error until a match was obtained between the simulated and the real deformed shapes. For the T4 sample, a match was achievable by using the following pressure (p) distribution as a function of distance (x) from the centre of the coil:

$$p = p_0 \exp\left[-(x/\delta)^4\right] \qquad (2)$$

The parameters p_0 and δ were taken as adjustable parameters and varied within a range until a perfect match was obtained between the simulated and the real geometries, with $p_0 = 200$ MPa and $\delta = 11.4$ mm. Figure 2 shows the pressure distribution corresponding to these best-fit parameters.
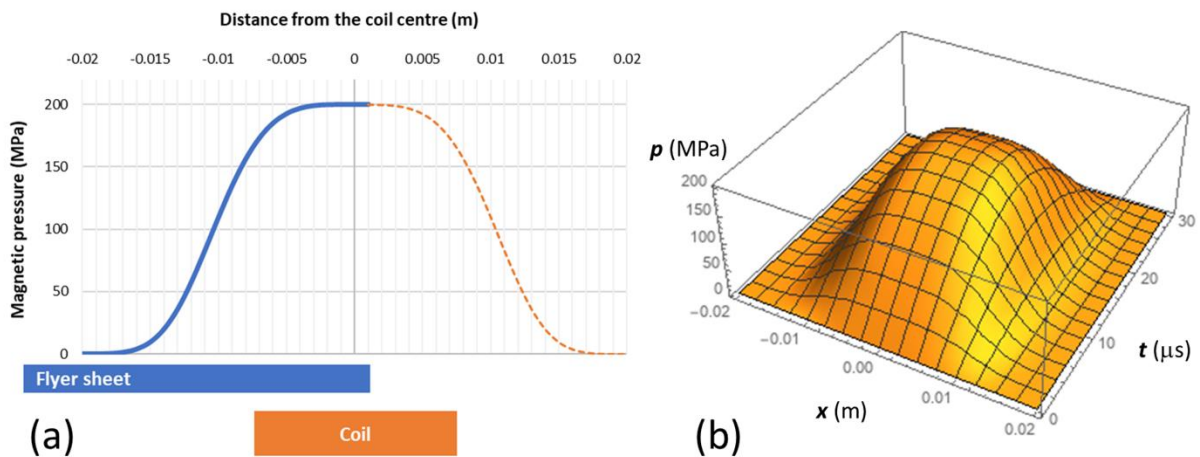
Figure 2. Amplitude of the assumed magnetic pressure as a function of distance from the coil centre (a) at the peak time (15 μs), and (b) for the entire loading time (the first pulse). The insets in (a) show the lateral dimension of the coil (15 mm width) and the position of the edge of the flyer (with a 1 mm offset) with respect to the coil axis.

Table 2. Material parameters assumed for finite element modelling

Property	Value	Unit
Density, ρ	2700, 2750*	kg m^{-3}
Thermal conductivity, κ	151	W m^{-1} K^{-1}
Specific heat capacity, c_p	900	J kg^{-1} K^{-1}
Thermal diffusivity, $\alpha = \kappa/(\rho c_p)$	6.21×10^{-5}	m^2 s^{-1}
Thermal expansion coefficient, β	2.32×10^{-5}	K^{-1}
Young's modulus, E	72.4, 80*	GPa
Shear modulus, G	26.2*	GPa
Poison's ratio	0.33	-
EOS parameters*:		
Grüneisen coefficient, γ_0	1.97	-
c_0	5.24×10^5	m/s
s	1.4	-
Johnson-Cook parameters:		
Melting temperature, T_m	650	°C
Reference temperature. T_{ref}	25	°C
Thermal softening exponent, m	1	-
A (T4) | A (T6)	190 | 300	MPa
B (T4) | B (T6)	300 | 200	MPa
Strain hardening exponent, n	0.5	-
Strain-rate hardening coefficient, C	0.01	-

* Used for sensitivity analysis (section 3.3)

3. Results of modelling

3.1. Deformation of the specimens

Figure 3 shows the deformation pattern in the T4 specimen, as well as the evolution of the equivalent plastic strain (PEEQ) during the impact. The outer solid contour in Fig. 3c (orange line in colour version) corresponds to the edge of the modelled specimens after impact. As shown in the figure, there is an excellent match between the real and the simulated boundaries of the deformed plates, using the pressure distribution function in Eq. (2) with a peak pressure of 200 MPa. A more detailed description of the distribution of plastic strain, especially at the interface, as well as diagrams showing FEM mesh distortion will be given in the following sections, e.g. in Fig. 4a. Also, an unmasked closeup of the interface of the same specimen is shown in Fig. 13.
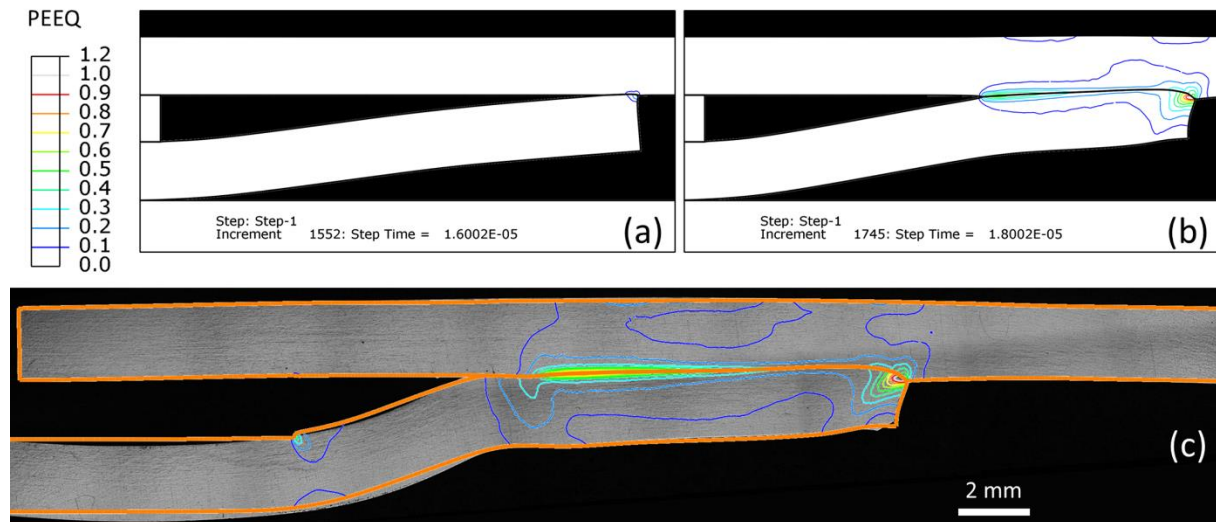
Figure 3. Deformation of the T4 specimen simulated at (a) 16 μs, (b) 18 μs, and (c) 50 μs after the start of loading. The inner contours indicate distribution of the equivalent plastic strain. The outer solid contour (orange in the colour version) in (c) corresponds to the FEM feature edges, superimposed on the real cross-section of the plates after EMPW.

3.2. Impact kinetics

Figure 4 shows the kinetics of the impact during EMPW, and the temperature distribution shortly after the impact. Figure 4a shows the nodal temperature (NT11) and the deformed mesh at 50 μs after loading. The temperature rise shown in Fig. 4a results from the dissipation of plastic work which occurs mainly over a period of about 4 μs. The plastic work is calculated for the entire model and saved as a default history output by ABAQUS, Fig. 4c. This characteristic process time corresponds to a thermal diffusion distance ($\sqrt{\alpha t}$) of about 15 μm, which is significantly smaller than the characteristic dimensions of the specimen, hence implying the process to be almost fully adiabatic. This assumption would also be valid for individual elements, which are larger than 20 μm in this study. It should be noted, however, that the element size has a significant influence on the maximum nodal temperature, plastic strain, and the horizontal (*x*) component of velocity at the interface. This effect will be discussed in the next section.

As shown in Fig. 4e, the initial impact velocity at the first point of contact (node 'S') is about 350 m/s. At this point, the contact angle is about 5°. The contact angle is calculated manually from the instantaneous coordinates of the corresponding surface nodes on the flyer and target plates. With the progress of the process, the impact velocity decreases to 270 m/s, and the contact angle increases to a maximum value of about 15° around node 'E'. The velocity of the contact point, v_c, shows the same trend (Fig. 4b). This characteristic velocity drops to less than half of its initial value (>4000 m/s) towards the end of impact. As mentioned before, variability of the impact angle and the characteristic velocities (v_y and v_c) is a unique feature that distinguishes EMPW from explosive welding.
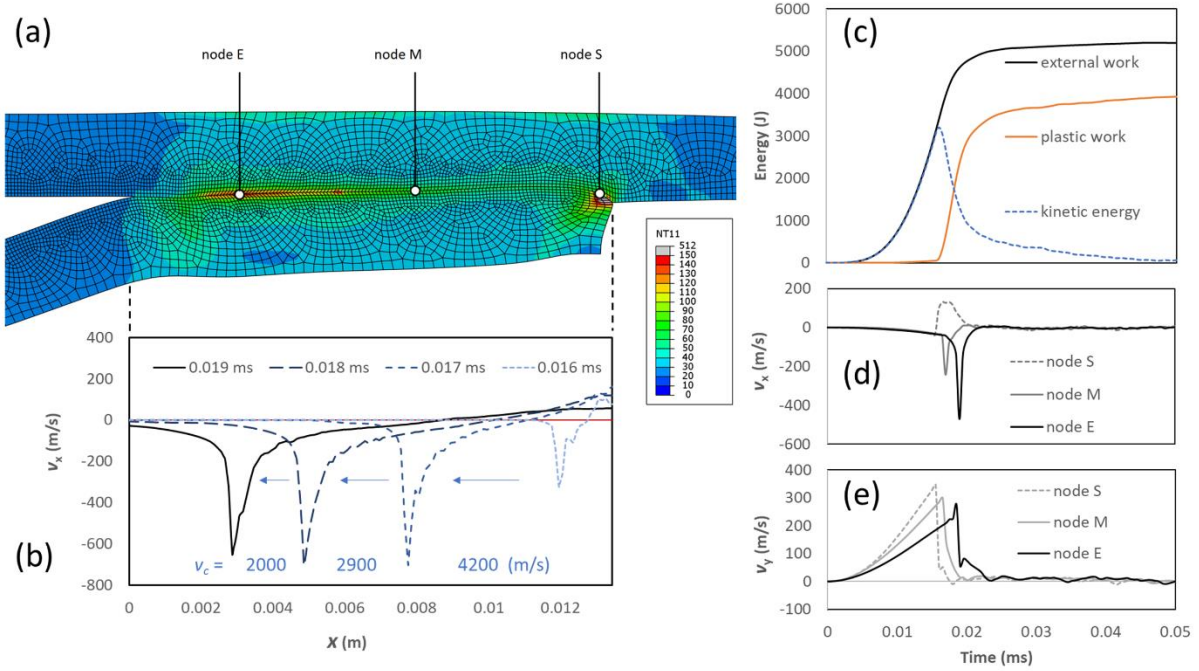
Figure 4. Calculated distribution of temperature (in Celsius) at 50 μs (a), horizontal component of the velocity of the interfacial nodes at different times during the impact (b), history of the kinetic energy (c), and history of the horizontal (d) and perpendicular (e) components of nodal velocities at three different locations.

3.3. Sensitivity to material parameters

Depending on the alloy grade and manufacturing steps, the material parameters can vary within a range. Moreover, the results of modelling can be influenced by the modelling approach, e.g. when using linear elasticity as opposed to equation of state (EOS). To quantify the influence of the variations in material properties, simulations are performed for alternative values of Young's modulus and density, as well as for a case where the elastic response of the material is modelled by using an EOS (Table 2). Figure 5 shows the results of the simulations with alternative parameters and assumptions. As shown in the figure, there is little deviation from the reference case ($E = 72$ GPa, $\rho = 2700$ kg/m^3) by changing the parameters. Therefore, the results of simulations throughout this study and the corresponding interpretations should

16

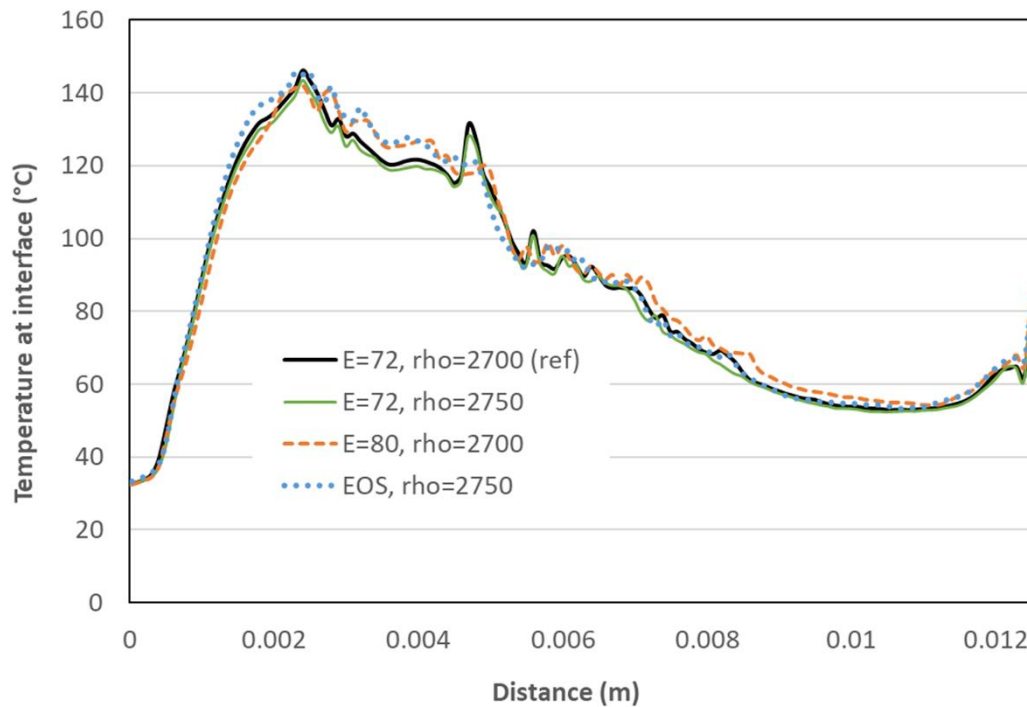be applicable to all aluminium alloys whose properties fall within the examined range of these properties.

Figure 5. Calculated strain profiles along an interfacial path on the target (substrate) for four different sets of assumed material properties.

3.4. Mesh sensitivity

The simulations presented so far correspond to a non-uniform mesh with a minimum element size of 100 μm around the contact region. The results show, however, that the plastic deformation is highly inhomogeneous, especially around node 'E' at the interface (Fig. 4a). Therefore, the calculated field variables (i.e. the equivalent plastic strain and temperature) only represent the average values for the corresponding elements; they can change substantially with the reduction of the element size. This is shown in Fig. 6, where the interfacial strain profiles are plotted for three mesh configurations, 1, 2 and 3, with the minimum element size of 100, 50 and 20 μm, respectively. The mesh configurations shown as insets on the right of the figure correspond to the same interfacial location (around node 'E'

17

for mesh 1, Fig. 4a) and the same time (19 μs) after impact. Note that at this time the impact is still in progress, hence there is a difference between the interface geometries shown in Fig. 4a and Fig 6. The figure shows that the overall level of the interfacial plastic strain increases substantially with decreasing the element size. It is also interesting to note that decreasing the element size to 20 μm results in the emergence of qualitatively different deformation patterns that are indicative of material jetting. These patterns would not be captured in the models with coarser elements. Moreover, the emergence of jetting was found to be associated with a prominent increase in the amplitude of the 'horizontal velocity spikes' as shown in Fig. 4b. In the current analysis, further decrease of the element size would result in excessive mesh distortion and numerical instability.
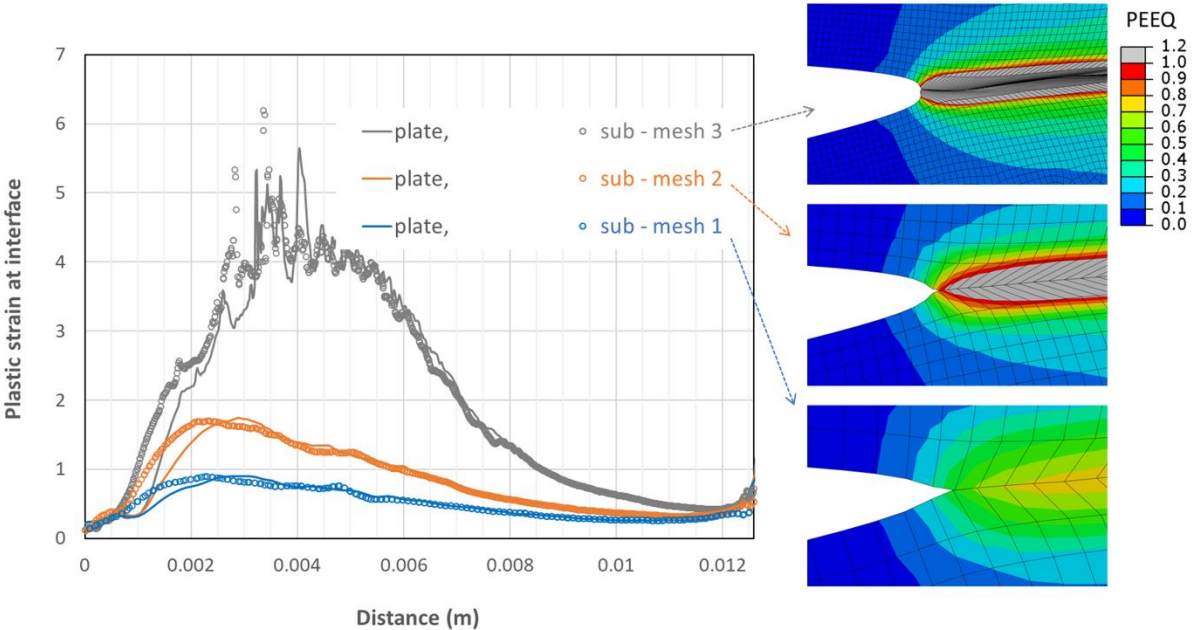

Figure 6. Calculated strain profiles along an interfacial path on the flyer and the target (substrate) for the three mesh configurations of 1, 2 and 3, with the minimum element size of 100, 50 and 20 μm, respectively. The insets show a close-up of the same interfacial location for all three configurations at 19 μs after the start of loading (i.e. 4 μs after the initial contact).

The uncertainty in the calculation of the interfacial plastic strain, because of mesh sensitivity, can be alleviated in the calculation of the interfacial temperature. This can be done through an analytical treatment as explained below, starting with the following energy balance:

$$fr\sigma d\varepsilon = \rho c_p dT \tag{3}$$

where f is the inelastic heat fraction (assumed to be 0.9 throughout this study), and r is a correction factor (>1) to compensate crudely for thermal effects due to thermo-elasticity, friction, viscous dissipation, and heat conduction. Assuming a Johnson-Cook relation without rate-dependency (i.e. $C = 0$ for simplicity), separation of variables and integration gives the temperature as a function of plastic strain as follows:

$$T = T_m - (T_m - T_{\text{ref}})\exp\left[-\frac{A\varepsilon + B\varepsilon^{n+1}/(n+1)}{\rho c_p(T_m - T_{\text{ref}})/(fr)}\right] \tag{4}$$

Figure 7a shows a plot of the above relation with the parameters given in Table 1. For comparison, the figure also shows the results of the corresponding FEM simulations. It is clear that a finer mesh is expected to produce physically more exact results with respect to spatial resolution of the thermal and mechanical field variables. On the other hand, a coarser mesh would be associated with less distortion and hence lead to a more accurate correlation between plastic strain and temperature under a purely adiabatic condition with no additional thermal effects. Thus, the figure includes the FEM results for all three mesh configurations. An important property of this model is that the temperature approaches the melting point asymptotically. This is because the additional thermal effects are incorporated as a coefficient in Eq. (3) for simplicity. By considering the thermal effects as additional terms on the left-hand side of Eq. (3), the temperature can exceed the melting point. In that case, however, the simple analytical solution, Eq. (4), will not be available. For the purpose of the present analysis, the analytical model can still be useful as it provides a basis to estimate interfacial

temperatures, with respect to the extent of thermal softening and the possibility of adiabatic shear instability (ASI).

Figure 7c shows the effect of element size on the maximum plastic strain as obtained from FEM simulations, and the corresponding temperature as calculated from Eq. (4). In view of these results, the maximum strain rate is expected to reach values in order of 10^6 1/s when the element size approaches zero. However, the correlation between the plastic strain and the element size is highly non-linear, so that an estimation of the maximum strain and strain rate at zero element size is not feasible. This is so, also because the scattering of the calculated strains is more prominent for finer mesh configurations. Therefore, extrapolation of the maximum strain to zero element size would be futile. This is nevertheless not the case for temperature. In view of the asymptotic form of Eq. (4), the maximum temperature for infinitesimal elements would be expected to reach temperatures around the melting point. As will be discussed later in more detail (section 5), this result demonstrates that the impact will be associated with extreme thermal softening, and that ASI will be inevitable for the examined cases. As mentioned above, the model is too simple to predict melting at zero element size, but the experimental results show no indication of melting (section 4). Therefore, it can be concluded that bonding in the examined systems does not require melting.
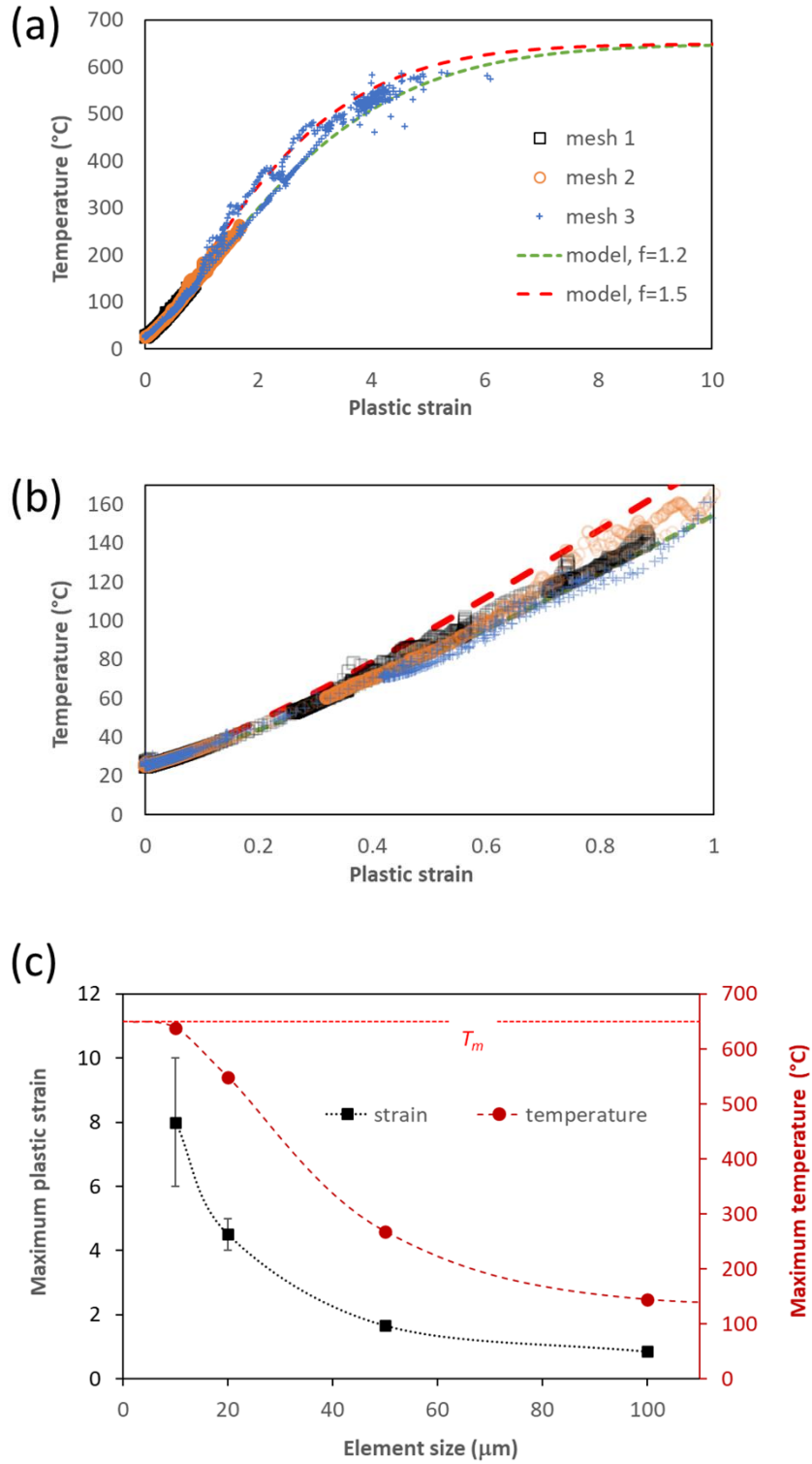
Figure 7. Calculated correlation between the temperature and plastic strain (a), its close-up near the origin (b), and the correlation between the maximum plastic strain / temperature and the element size (c). The analytical model in (a) and (b) relates to Eq. (4) with the parameters given in Table 1.

4. Experimental results

4.1. Bonding and mechanical characterisation

The debonding tests showed that welding could be successfully achieved for the examined aluminium alloy in both T4 and T6 temper conditions. Microscopic observations showed a region of intimate contact (bonding) of ~7.1 mm of the total contact length of about 12 mm for the T6 sample, and ~8.4 mm for the T4 sample.

Figure 8 shows that the overall hardness of the joint region was raised as compared to the base material, which had an original hardness of ~80 Hv (black dashed line in Fig. 8b) in the T4 condition. As seen from Fig. 8b, the hardness was increased to 90-120 Hv along the centreline of both the flyer and the target plates around the joint. Moreover, the hardness profiles on the two plates show opposite trends, i.e. increasing along the welding direction in the centreline of flyer plate, while decreasing in the target plate. Figure 8c shows the hardness profile along a transverse direction, indicating a maximum of about 120 Hv at the bond line. These profiles are in qualitative agreement with the simulations in view of the strain hardening effect, i.e. larger plastic strains should result in higher values of hardness.

After a post-weld ageing to the T6 temper, the base material hardness reaches ~110 Hv (red dashed line in Fig. 8b). Further increase in hardness (up to around 125 Hv) is observed around the joint region, which implies a noticeable effect of plastic deformation on the subsequent precipitation hardening. On the other hand, the difference in hardness along the centrelines of the flyer and target plates is not significant. All hardness values after T6 post-weld treatment are consistently higher across the joint as compared to the as-welded T4 condition. This is so, especially for the region far way the weld interface (i.e. 1 to 2 mm from the joint interface).
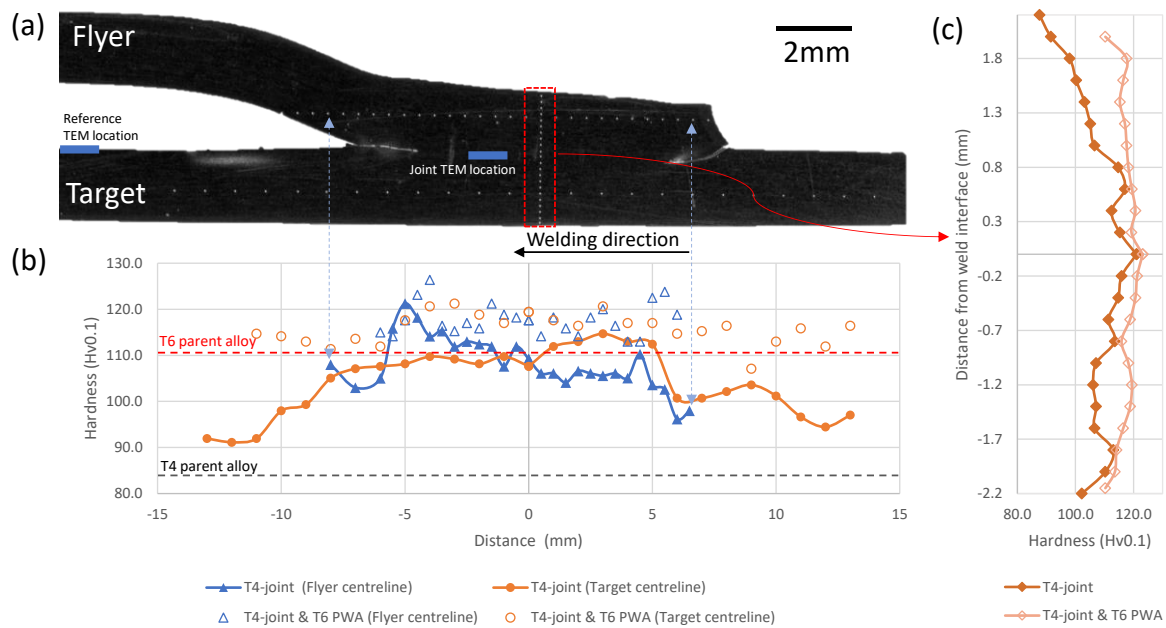
Figure 8. Hardness profiles on the cross-section of the welded T4 sample: (a) optical image of the cross-section of the sample marked with the location of hardness testing points, (b) the corresponding hardness profiles along the centreline of flayer and target plates before (T4-joint) and after T6 post-welding ageing (T6 PWA), and (c) hardness profiles in the transverse direction. the solid symbol curve represents the hardness after welding in the T4 condition, and the open symbol represents the hardness after T6 post-welding ageing condition. The (blue) rectangular markers in (a) show the locations of the samples taken for TEM studies (Figs 10 and 11).

4.2. Microstructural characterisation

The microstructure of this material is typical of a high strength 6000-series extruded alloy. A high density of Fe/Mn based dispersoids prevents recrystallisation, creating a peripheral coarse grain structure at the surfaces and a fine fibrous texture at the core. The majority of the strengthening comes from the precipitation of metastable Mg-Si-Cu structures when the material (which is quenched immediately after extrusion) is aged. There are many structural possibilities for the hardening precipitates – Andersen et al. (2018) list 13 possible precipitate

phases in the Al-Mg-Si(-Cu) system. In this alloy, the majority of precipitates were identified

as either Q', β", or a disordered L phase as shown in Fig. 9.
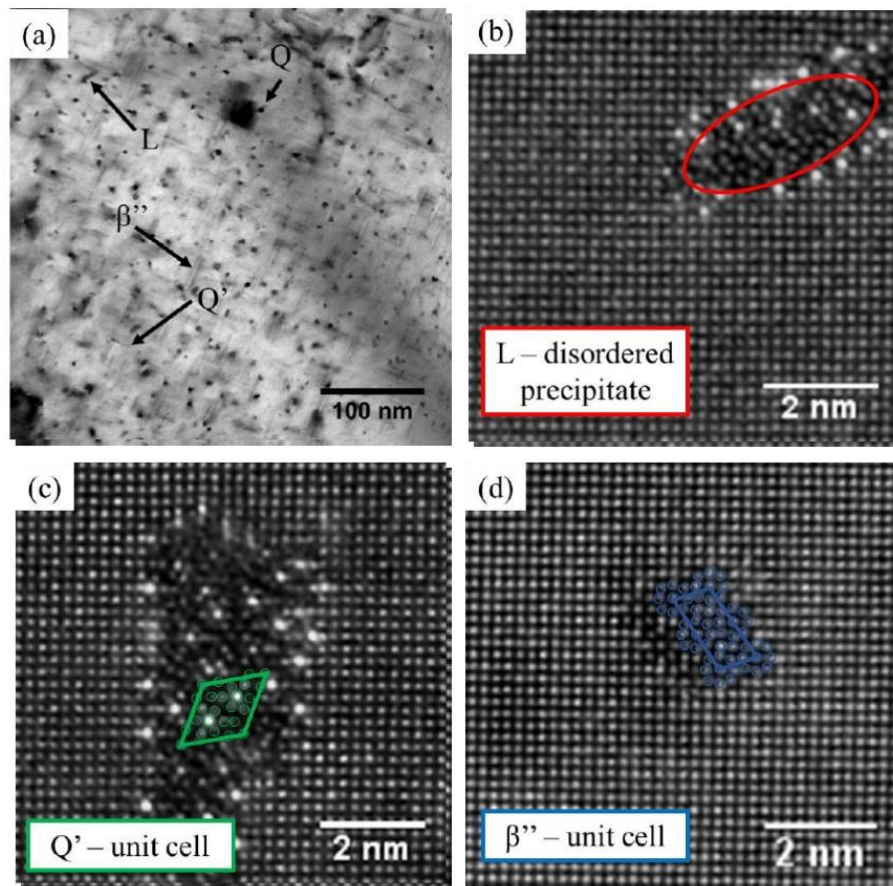

Figure 9. (a) Bright-field TEM image of precipitates in the un-bonded T6 material (b-d) High

resolution ADF-STEM images of various precipitates with (c) overlayed Q' unit cell

configuration (Saito et al., 2014) (d) overlayed β" unit cell configuration (Andersen et al.,

1998).

To investigate the effect of the EMPW process on the grain structure, EBSD analyses were

performed on both the joint and the base material regions. Figure 10 shows an overview the

EBSD results, where the grain structure around the bonded interface can be compared to that

of the base material. The inverse profile figure (IPF) map with high angle boundaries (HABs,

θ>15°) in Fig. 10a shows that the grains in the vicinity of the interface are highly deformed

and skewed along the welding direction. There is also an indication of fine recrystallized grains at the interface, Fig. 10b. A high density of HABs can be observed even in the areas away from the joint interface. However, locations closer to the joint interface are dominated by significantly higher densities of HABs and sub-grains (red lines in Fig. 10c). Quantitative measurement of the misorientation angle distributions, as performed on a large area of joint region and base material, indicates a much higher HAB (15° to 65°) density from, 5.2×10^6 mm^{-2}, as compared to the base material, $8.3 \times 10^5 \, mm^{-2}$. The base material, as seen from the IPF and misorientation maps (Figs 10b-c and e-f), shows a typical extrusion texture.

Figures 10d & g show the kernel average misorientation (KAM) with a 5° threshold angle for the joint interface region and the base material, respectively. It is clear that the high kernel values (from 1 to 5) are predominant in the regions around joint interface rather than the base material. Zero KAM locations (blue area in Fig. 10d) with high misorientation angle boundaries ($\theta > 15°$) can be an indication of recrystallization.
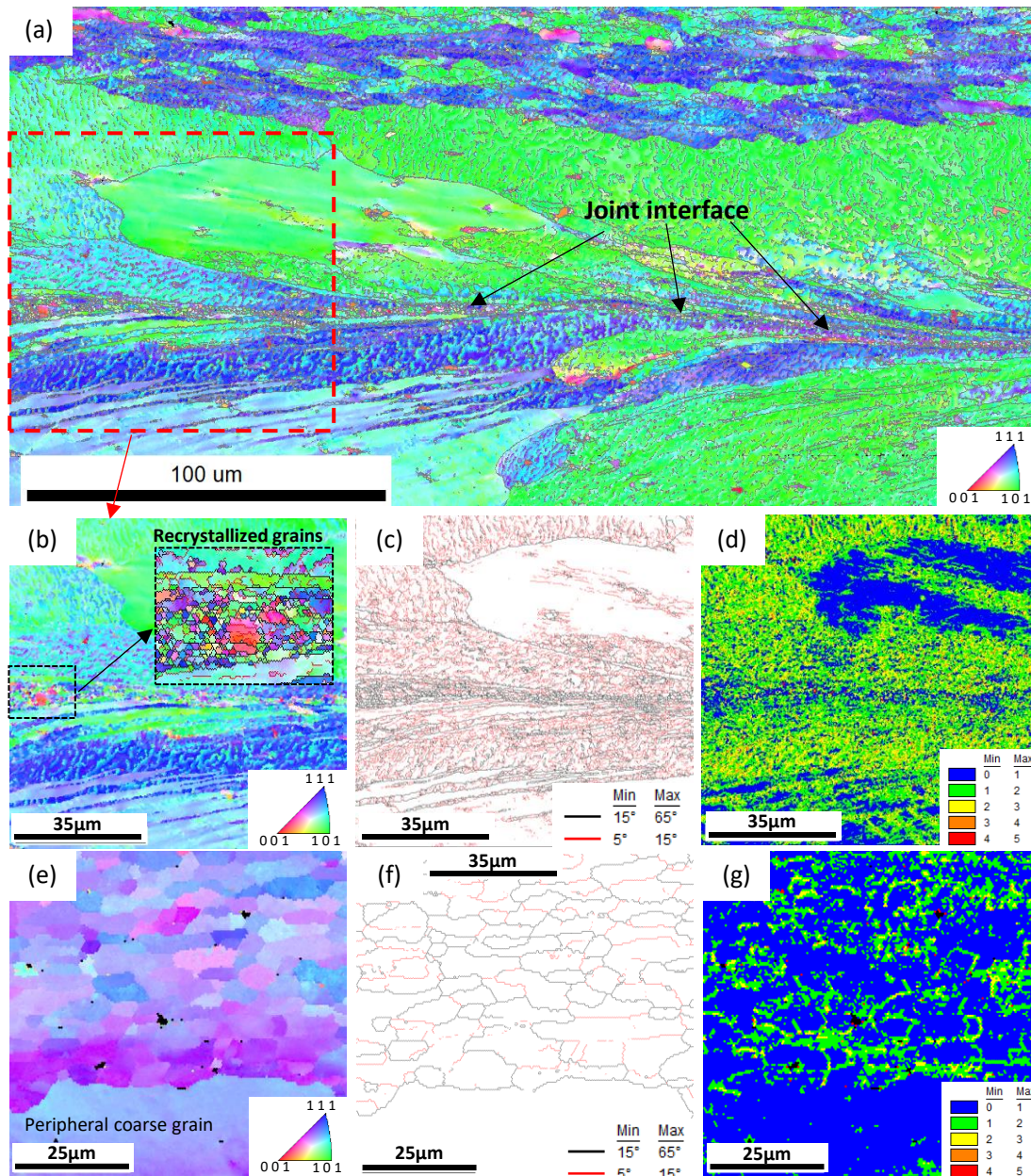
Figure 10. EBSD results: (a) Inverse pole figure (IPF) map with of the region near the joint interface in the welded T4 sample (the grey lines represent the high-angle grain boundaries, θ>15°); (b), (e) IPF map, (c), (f) misorientation map and (d), (g) kernel average misorientation map of the area marked in (a) and of the base material, respectively. Black lines are high-angle (θ>15°) boundaries, red lines are low angle (5°<θ<15°) boundaries.

Figure 11 shows bright-field TEM images of two different locations, reference and joint (as marked in Fig. 8a) in the T4 sample. The low magnification TEM images in Fig. 11a & b show a prominently higher dislocation density in the joint region, and a complex sub-grain structure. The difference in dislocation density between the reference and joint regions can clearly explain the measured difference in the hardness between these regions. Figure 11b also shows a 'patchy' dislocation cell structure in the highly deformed joint region. Lee and Chen (2006) provide examples of this feature, which is commonly found in high strain-rate deformation processes. In the T4 condition, no resolvable hardening precipitates were expected in the microstructure, and none were observed in either the reference region or in the vicinity of the joint (Fig. 11d & e). Figure 11c also indicates some recrystallisation in the T4 sample after joining (T4 joint) and T6 post welding treatment (T6 PWA). Although the grain structure is clear, there is still a high density of dislocations and some parts with no indication of recrystallisation. Figure 11f shows an evidence of fine precipitates in the joint region.
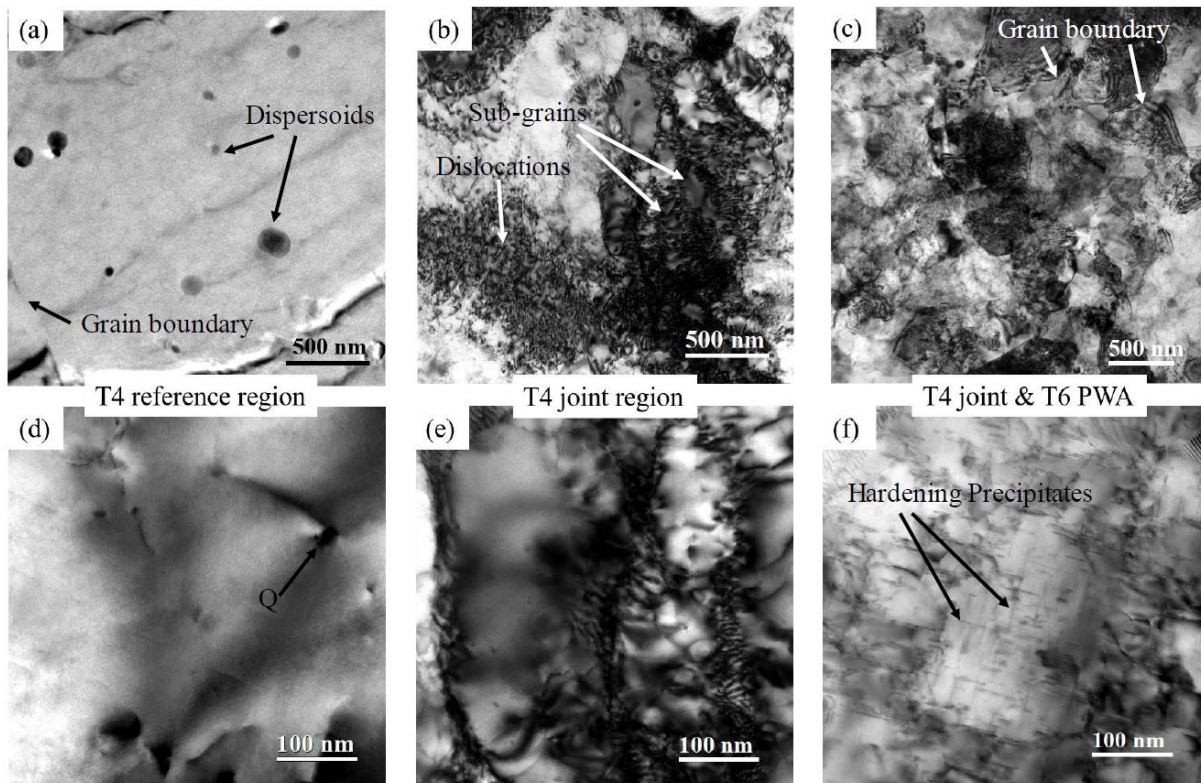
Figure 11. TEM (bright-field) images of the welded T4 sample at different magnifications: (a) and (d) show grain boundaries and dispersoids in the reference region, (b) and (e) show high density of dislocation and smaller grains in the vicinity of the joint region, (c) and (f) show recrystallization and fine precipitates in the joint region after post-weld T6 ageing treatment.

Figure 12 shows TEM images of different locations in the T6 sample. In this sample, the TEM image from the reference and joint regions (Fig. 12a & b) also indicate a significant increase in dislocation density after joining. At higher magnifications, the TEM image from the reference region (Fig. 12d) shows the typical distribution of β'', Q' and L precipitates in the T6 condition. As shown in Fig. 12e, it is interesting to note that the high density of needle-like β'', Q' precipitates seen in the reference region are no longer observable after joining, with some regions appearing to show no precipitates at all. The remaining precipitates appear to be globular and are likely to be equilibrium phases (e.g. Mg_2Si or Q) precipitated on features like

dislocations before the quench after extrusion (similar to those seen in Fig. 11d). Once an additional T6 ageing treatment is applied to the T6 welded sample, less recrystallisation can be observed; compare Figs 11c and 12c. Zurob et al. (2002) attribute this to the precipitates providing a Zener pinning force to slow down or even halt the process of recrystallisation. A higher magnification TEM (Fig. 12f) shows that the precipitates are very coarse, which is consistent with the hardness measurements, showing no increase in hardness at the joint region (Fig. 8).
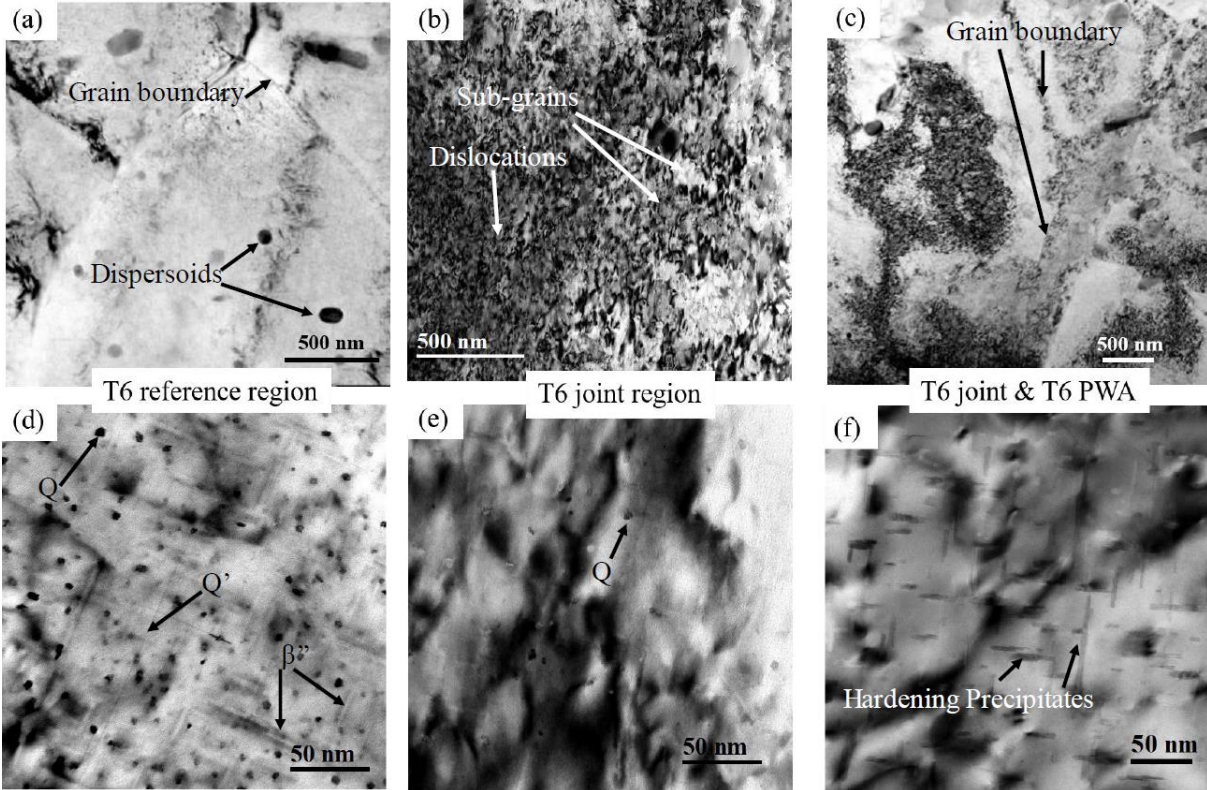

Figure 12. TEM images of the welded T6 sample in the reference region at (a) low and (d) high magnifications, showing β''and Q' precipitates, and in the joint region at (b) low and (e) high magnifications, showing globular (possibly equilibrium phase) precipitates; (c) and (f) show partial recrystallization and coarse precipitates after post-weld T6 ageing, respectively.

5. Implications for bonding

5.1. Bonding criterion

As mentioned in the introduction, the mechanism of bonding in EMPW has been widely discussed in the literature. The previous studies have identified several factors and features with a possible role in bonding. These include material jetting, formation of a wavy interface, and localised melting. In addition to the experience obtained from these EMPW-specific studies, conditions that lead to successful bonding can be discussed in view of the existing experience on similar solid-state processes, such as explosive welding and cold spraying, in which bonding occurs as a result of high-velocity impact and severe plastic deformation at the interface. In those other processes, various bonding criteria have been discussed at two different levels: (1) at the process level, i.e. considering the impact conditions (the impact velocity and the impact angle), and (2) at the micro-level, i.e. considering the microscopic conditions at the interface, such as the interfacial strain or temperature. A comprehensive bonding criterion should incorporate the relevant parameters at both levels, so that the critical conditions at the micro-level become a basis to work out those at the process level.

In explosive welding, the bonding criteria are often formulated and expressed solely in terms of the impact velocity and the impact angle. The relevance of the latter is interpreted in view of the velocity of the contact point, v_c. An established criterion in explosive welding is that bonding can be achieved only if v_c is below the speed of sound in the solid. The simulation results suggest that this condition is typically fulfilled in EMPW (Fig. 4b). This is so because, unlike in explosive welding, the impact angle and the corresponding v_c in EMPW varies over a relatively wide range; it is thus likely that the condition is fulfilled at least in a part of the contact zone. The role of the impact velocity is more intricate and should be discussed in view

of the microscopic conditions, i.e. the thermomechanical history of the interface at the micro-level. This is explained below.

A prime assumption for solid-state bonding is that the surface oxide layers should be broken up or removed from the system, so that there is a possibility for clean metallic surfaces to be in tight contact to form a metallic bond. A way to achieve this, is to stretch the interface to a certain level of strain under compressive hydrostatic pressure, so that the oxide layers are broken while the microscopic gaps between the oxide-free surfaces are closed. In high-velocity impact processes, this can happen through generation of localised shear forces at the interface, leading to large interfacial plastic strains, which is often associated with jetting and adiabatic heat generation. The latter effect in turn results in thermal softening, which can further facilitate localised plastic deformation and lead to adiabatic shear instability (ASI). Assadi et al. (2003) show that in cold spraying, there is a distinct transition to ASI with increasing the particle impact velocity, which coincides with the corresponding critical velocity for bonding. Therefore, ASI has been taken as a criterion for particle bonding to predict the critical velocity as a function of material properties. Since the ASI criterion takes account of both work hardening and thermal softening during plastic deformation, the critical velocity can be linked to both thermal and mechanical parameters. However, quantitative simulation of ASI is not straightforward, mainly because of the high sensitivity of the results to the mesh size (Fig. 6). In the present study, extrapolation to zero element size (Fig. 7b) shows that ASI is likely to occur (i.e. difficult to avoid) for the given set of process and materials parameters.

Alternatively, a bonding criterion can be conceived in view of the trend of plastic strain profiles along the corresponding contact surfaces as calculated using a 'medium-size' mesh (mesh 2 in Fig. 6). Figure 13 shows these profiles for both the flyer and the target plates of the T4 sample, scaled to the real length, and superimposed on the cross-section, of the welded

coupon. It can be noted that (a) the boundaries of the welded interface coincide with the extrema of the strain profiles, and (b) the strain on both the flyer and the target plates are more or less equal within the region between the extrema. The latter point implies conformal deformation in the welded region, i.e. there is little relative displacement of the contact surfaces in this region. In view of these observations, bonding in EMPW can be conceived to occur when the interfacial strains on both surfaces exceed a nominal threshold value (relating to an expected ASI at the hypothetical zero element size) at the same time.
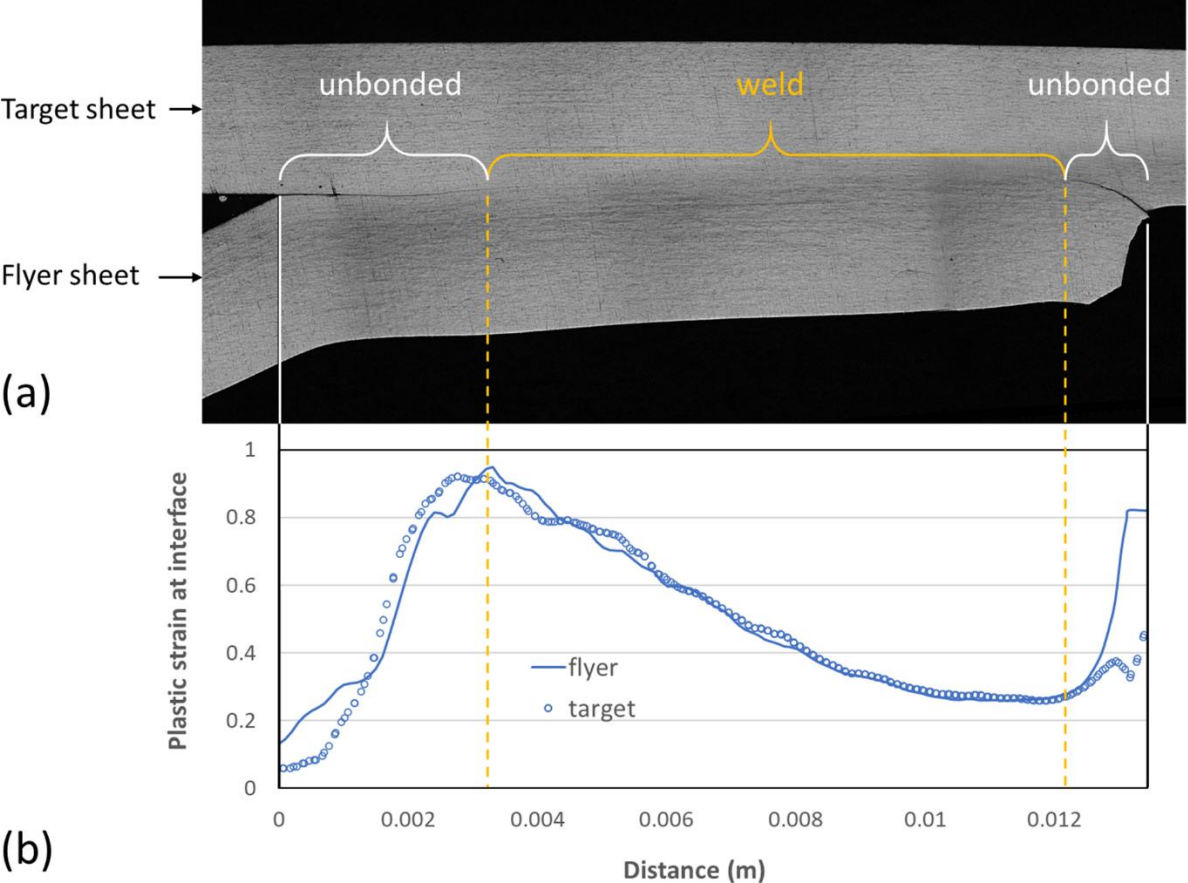

Figure 13. An image of the cross-section of the T4 specimen (a) and the corresponding strain profiles along the paths on the interacting surfaces as obtained from FEM simulation with an element size of 100 μm (b).

5.2. Parameter study

In view of the above criteria, the influence of process parameters on the occurrence and extent of bonding in EMPW can be investigated. Figure 14 shows examples of a parameter study for two cases in which (a) the airgap, and (b) the material properties are varied. In the case where the airgap is increased from the original value of 2 mm, the overall level of strain on both plates is increased, and vice versa (Fig. 14a). However, the increase in the overall strain is associated with a decrease in the distance between the two extrema, suggesting that the overall length of the bonded zone will decrease by increasing the airgap distance above 2 mm. Moreover, the respective profiles on the surfaces of the plates deviate from one another at 4 mm, indicating alleviation of conformal deformation with increasing the airgap. This implies that the bonding quality may degrade when the airgap is excessively increased. On the other hand, decreasing the airgap to 1 mm will result in a better match between the profiles, i.e. implying conformal deformation throughout the entire contact region. However, the overall amount of plastic strain in this case is reduced to less than a half of that in the case of 2 mm airgap. This is mainly because of the reduced impact velocity (shorter acceleration time) and suppressed ASI. In this case, therefore, bonding would be expected to occur either over a much shorter distance, or not at all. This is simply because the interfacial strain barely reaches the required threshold value, which is for the given mesh around 0.3. This value is obtained in view of the comparison between the simulations and the experimental results (Fig. 13). In the case where the material properties are changed from T4 to T6 condition, both the level of strain profiles and the distance between the two extrema are reduced (Fig. 14b). However, the deformation remains conformal for the harder material (T6) and the strain does not fall below the threshold value within the region bound by the extrema. Therefore, bonding is expected to occur for the T6 sample, although over a smaller distance as compared the T4 sample. This prediction is also quantitatively consistent with the experimental observations,

confirming a welded length of about 7 mm for the harder material. Several other parameters –
e.g. the thickness or shape of the flyer plate and the magnitude or duration of the magnetic
pressure – can be studied in this way. The obtained correlations can then be used to construct
a parameter selection map, such as that for cold spraying as stated by (Assadi et al., 2011).
These maps will link the primary process parameters to the properties and extent of welding,
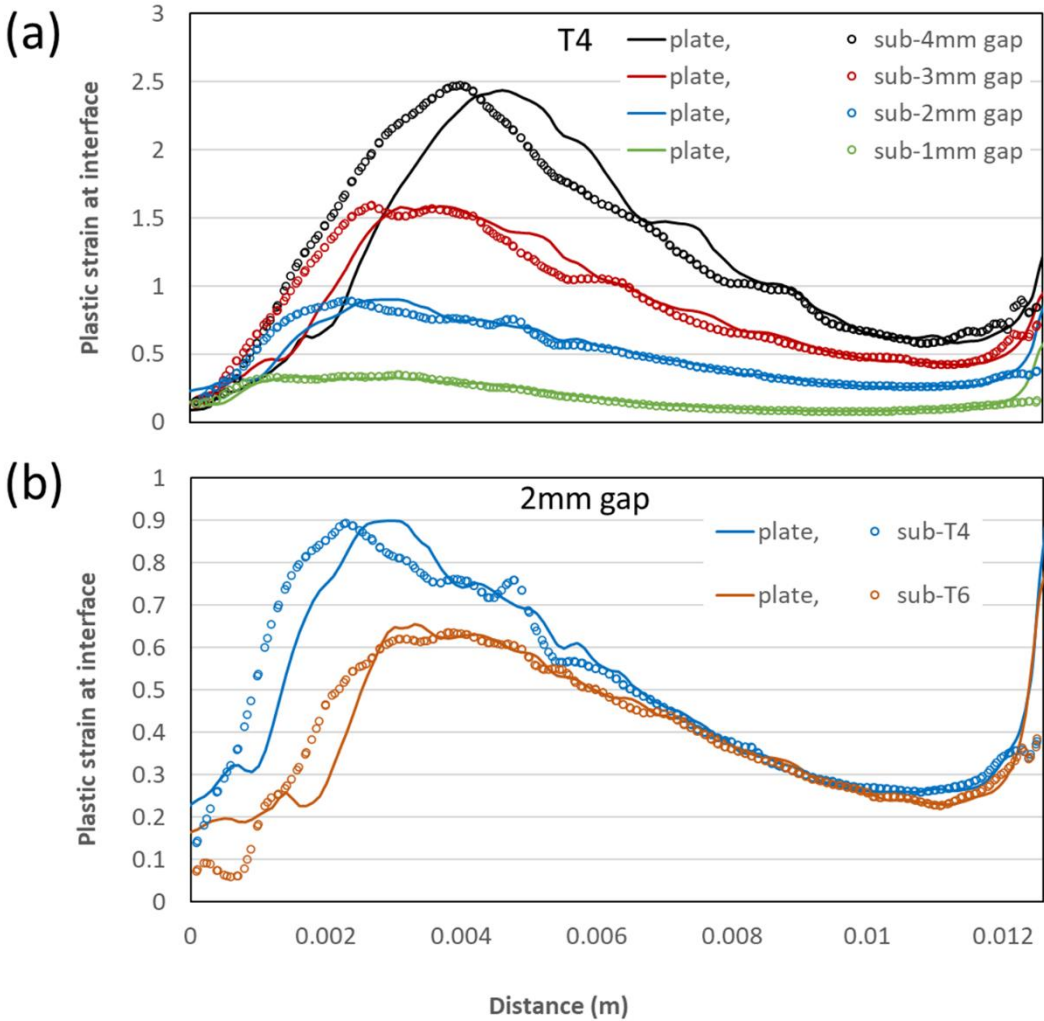and so, provide a basis for optimisation of the EMPW process.

Figure 14. Calculated strain profiles along the paths on the interacting surfaces, as obtained
from FEM simulations with an element size of 100 μm, for (a) the T4 specimen with four
different airgap distances of 1-4 mm, and (b) for a fixed airgap of 2-mm distance and different
specimens (T4 and T6).

6. Discussion of bonding and microstructural changes

As expected, the samples became significantly harder than the parent alloy after EMPW, because of the impact-induced plastic deformation (work hardening) and microstructural changes. This effect was more pronounced around the joint region in the T4 sample. A shorter bond length was observed experimentally when using the same set of parameters for the T6 sample. This is due to higher resistance to viscoplastic flow and hence a lower level of plastic strain at the surface of the interacting plates. A higher plastic strain at the interface could generally lead to a better metallic bonding. This observation agrees well with the result of numerical simulations.

EBSD results indicate that the process is associated with severe plastic deformation, manifested by the generation of a significantly high density of HABs around the joint region. The grains in this region are highly elongated, which is consistent with the predicted values of up to ~10 (Fig. 7). Hughes and Hansen (1997) and Sun et al. (2011) propose that the formation of HABs are commonly attributed to the accumulation of dislocations and formation of dense dislocation walls (DDW), which subdivide the original grains. Lin et al. (2016) report that at higher amounts of plastic strain in the joint interface, the sub-grains are gradually transformed into dynamically recrystallised (DRX) grains. This feature has also been observed in the TEM of the present samples (Fig. 11).

The TEM results provide further evidence for the above interpretation, and so, a further basis understanding of the effect of the EMPW process on the microstructure. TEM analysis revealed high density of dislocations and a very fine grain structure near the joint interface. These features are characteristics of high strain-rate and severe plastic deformation. Recrystallisation and grain refinement has been widely reported in other large-displacement deformation processes. Zhilyaev et al. (2008) and Wu et al. (2002) provide examples in severe plastic deformation (SPD) and ultrasonic shot peening (USSP), respectively. Faraji et

al. (2018) and Lee et al. (1999) attribture the increase in strength in these processes to the Hall-Petch effect as well as work hardening. The high density of HABs (Fig. 10a) is also consistent with the observed increase of the hardness of the joint region as compared to the base material.

The distribution of precipitates in the reference area of the T6 material (Fig. 12d) is a mixture of Q', β" precipitates and globular equilibrium phases. As shown in Fig. 12e, the globular precipitates remain present after EMPW, but the previously dense distribution of needle-like Q' and β" precipitates is less obvious. This is consistent with previous studies on aluminium alloys undergoing high strain-rate deformation. For example, Yang et al. (2016) and Ye et al. (2019) have made similar observations and attributed this to the high level of plastic strain induced by the impact during joining, leading to the dissolution of these precipitates. During the EMPW process, the high strain rate impact deformation will break the thermodynamic equilibrium through introducing the great change of free energy for both matrix and precipitates. According to Ye et al. (2019), the dissolution of precipitates will happen once the energy difference between precipitates and matrix reaches a certain degree. At the same time, temperature rise can also facilitate the atom transfer and improve the kinetics of dissolution. Besides, the ageing behaviour of the precipitates appears similar to that of the base alloy even within the joint region.

These observations demonstrate that in EMPW of the studied aluminium alloy, bonding is associated with a high level of shear strain and significant microstructural changes near the joint. The high shear results in dissolution of the ageing precipitates, as well as in the formation of a complex network of dislocations and sub-grains. The latter is manifested as recrystallisation, i.e. formation of a fine grain structure upon subsequent ageing. For the materials and process parameters used in this study, there was no evidence of localised melting at the interface. These observations together with numerical simulations provide an

insight on how EMPW results in bonding and changes in microstructure, and so, a basis for prediction and controlling of the resulting material and the joint properties of hardenable aluminium alloys. These results can also provide an insight to EMPW of other metallic materials. However, transferring the results to other metallic systems (e.g. dissimilar steel/aluminium joints) will require separate quantitative analyses and careful consideration of the flow behaviour and the microstructural response of the respective materials to high-strain rate deformation, which can be substantially different from those considered in this study.

7. Conclusions

Plates of a high-strength aluminium alloy in the T4 and T6 temper conditions have been joined successfully by using electromagnetic pulse welding (EMPW). Microstructural studies showed that bonding in these samples was associated with significant microstructural changes, especially near the joint area. These changes include mechanically induced dissolution of precipitates, formation of dislocation networks, and recrystallisation. No evidence of melting was found for the employed set of materials and parameters. For the post-weld heat treatable material, a significant increase in the strength was observed, indicating the effect of plastic deformation on precipitation during the subsequent ageing treatment. Finite element modelling of the process was combined with the experimental observations to show that bonding could occur over a part of the contact region where the deformation was conformal, and adiabatic shear instability was likely to occur. Initial parameter studies confirmed the experimental observations on the optimum airgap distance and the length of the bonded interfaces for different samples.

References

Andersen, S.J., Marioara, C.D., Friis, J., Wenner, S., Holmestad, R., 2018. Precipitates in aluminium alloys. Adv. Phys. X 3, 1479984.

Andersen, S.J., Zandbergen, H.W., Jansen, J., Traeholt, C., Tundal, U., Reiso, O., 1998. The crystal structure of the β ″phase in Al–Mg–Si alloys. Acta Mater. 46, 3283–3298.

Assadi, H., Gärtner, F., Stoltenhoff, T., Kreye, H., 2003. Bonding mechanism in cold gas spraying. Acta Mater. 51, 4379–4394.

Assadi, H., Kreye, H., Gärtner, F., Klassen, T., 2016. Cold spraying–A materials perspective. Acta Mater. 116, 382–407.

Assadi, H., Schmidt, T., Richter, H., Kliemann, J.-O., Binder, K., Gärtner, F., Klassen, T., Kreye, H., 2011. On parameter selection in cold spraying. J. Therm. spray Technol. 20, 1161–1176.

Bataev, I.A., Tanaka, S., Zhou, Q., Lazurenko, D. V, Junior, A.M.J., Bataev, A.A., Hokamoto, K., Mori, A., Chen, P., 2019. Towards better understanding of explosive welding by combination of numerical simulation and experimental study. Mater. Des. 169, 107649.

Bellmann, J., Lueg-Althoff, J., Schulze, S., Gies, S., Beyer, E., Tekkaya, A.E., 2016. Measurement and analysis technologies for magnetic pulse welding: established methods and new strategies. Adv. Manuf. 4, 322–339.

Ben-Artzy, A., Stern, A., Frage, N., Shribman, V., 2008. Interface phenomena in aluminium–
magnesium magnetic pulse welding. Sci. Technol. Weld. Join. 13, 402–408.

Ben-Artzy, A., Stern, A., Frage, N., Shribman, V., Sadot, O., 2010. Wave formation
mechanism in magnetic pulse welding. Int. J. Impact Eng. 37, 397–404.

Chen, S., Daehn, G.S., Vivek, A., Liu, B., Hansen, S.R., Huang, J., Lin, S., 2016. Interfacial
microstructures and mechanical property of vaporizing foil actuator welding of
aluminum alloy to steel. Mater. Sci. Eng. A 659, 12–21.

Elsen, A., Groche, P., Ludwig, M., Schaefer, R., 2010. Fundamentals of EMPT-welding, in:
4th International Conference on High Speed Forming, March 9th-10th 2010 Columbus,
Ohio, USA. Institut für Umformtechnik-Technische Universität Dortmund.

Faraji, G., Kim, H.S., Kashi, H.T., 2018. Severe Plastic Deformation: Methods, Processing
and Properties. Elsevier.

Göbel, G., Kaspar, J., Herrmannsdörfer, T., Brenner, B., Beyer, E., 2010. Insights into
intermetallic phases on pulse welded dissimilar metal joints, in: 4th International
Conference on High Speed Forming. pp. 127–136.

Groche, P., Wagner, M.-X., Pabst, C., Sharafiev, S., 2014. Development of a novel test rig to
investigate the fundamentals of impact welding. J. Mater. Process. Technol. 214, 2009–
2017.

Hammerschmidt, M., Kreye, H., 1981. Microstructure and bonding mechanism in explosive
welding, in: Shock Waves and High-Strain-Rate Phenomena in Metals. Springer, pp.
961–973.

Hughes, D.A., Hansen, N., 1997. High angle boundaries formed by grain subdivision

mechanisms. Acta Mater. 45, 3871–3886.

Kapil, A., Sharma, A., 2015. Magnetic pulse welding: an efficient and environmentally friendly multi-material joining technique. J. Clean. Prod. 100, 35–58.

Kore, S.D., Date, P.P., Kulkarni, S. V., Kumar, S., Rani, D., Kulkarni, M.R., Desai, S. V., Rajawat, R.K., Nagesh, K. V., Chakravarty, D.P., 2011. Application of electromagnetic impact technique for welding copper-to-stainless steel sheets. Int. J. Adv. Manuf. Technol. 54, 949–955.

Kwee, I., Psyk, V., Faes, K., 2016. Effect of the Welding Parameters on the Structural and Mechanical Properties of Aluminium and Copper Sheet Joints by Electromagnetic Pulse Welding. World J. Eng. Technol. 04, 538–561.

Lee, T., Nassiri, A., Dittrich, T., Vivek, A., Daehn, G., 2020. Microstructure development in impact welding of a model system. Scr. Mater. 178, 203–206.

Lee, W.-S., Chen, T.-H., 2006. Rate-dependent deformation and dislocation substructure of Al–Sc alloy. Scr. Mater. 54, 1463–1468.

Lee, W.-S., Shyu, J.-C., Chiou, S.-T., 1999. Effect of strain rate on impact response and dislocation substructure of 6061-T6 aluminum alloy. Scr. Mater. 42, 51–56.

Li, J.S., Raoelison, R.N., Sapanathan, T., Hou, Y.L., Rachik, M., 2020. Interface evolution during magentic pulse welding under extremely high strai rate collision: mechanisms, thermomechanical kintetics and consequences. Acta Mater. 195, 404–415.

Lin, Y.C., He, D.-G., Chen, M.-S., Chen, X.-M., Zhao, C.-Y., Ma, X., Long, Z.-L., 2016. EBSD analysis of evolution of dynamic recrystallization grains and δ phase in a nickel-based superalloy during hot compressive deformation. Mater. Des. 97, 13–24.

McCune, R.C., Papyrin, A.N., Hall, J.N., Riggs, W.L., Zajchowski, P.H., 1995. An exploration of the cold gas-dynamic spray method for several materials systems. ASM International, Materials Park, OH (United States).

Nassiri, A., Chini, G., Kinsey, B., 2014. Spatial stability analysis of emergent wavy interfacial patterns in magnetic pulsed welding. CIRP Ann. 63, 245–248.

Nassiri, A., Chini, G., Vivek, A., Daehn, G., Kinsey, B., 2015. Arbitrary Lagrangian-Eulerian finite element simulation and experimental investigation of wavy interfacial morphology during high velocity impact welding. Mater. Des. 88.

Nassiri, A., Abke, T., Daehn, G., 2019. Investigation of melting phenomena in solid-state welding processes. Scr. Mater. 168, 61–66.

Palmer, T.A., Elmer, J.W., Brasher, D., Butler, D., Riddle, R., 2006. Development of an explosive welding process for producing high-strength welds between niobium and 6061-T651 aluminum. Weld. Journal New York 85, 252.

Parchuri, P., Kotegawa, S., Yamamoto, H., Ito, K., Mori, A., Hokamoto, K., 2019. Benefits of intermediate-layer formation at the interface of Nb/Cu and Ta/Cu explosive clads. Mater. Des. 166, 107610.

Pereira, D., Oliveira, J.P., Pardal, T., Miranda, R.M., Santos, T.G., 2018. Magnetic pulse welding: machine optimisation for aluminium tubular joints production. Sci. Technol. Weld. Join. 23, 172–179.

Psyk, V., Risch, D., Kinsey, B.L., Tekkaya, A.E., Kleiner, M., 2011. Electromagnetic forming—a review. J. Mater. Process. Technol. 211, 787–829.

Raoelison, R.N., Buiron, N., Rachik, M., Haye, D., Franz, G., Habak, M., 2013. Study of the elaboration of a practical weldability window in magnetic pulse welding. J. Mater.

Process. Technol. 213, 1348–1354.

Raoelison, R.N., Sapanathan, T., Buiron, N., Rachik, M., 2015. Magnetic pulse welding of Al/Al and Al/Cu metal pairs: Consequences of the dissimilar combination on the interfacial behavior during the welding process. J. Manuf. Process. 20, 112–127.

Saito, T., Marioara, C.D., Andersen, S.J., Lefebvre, W., Holmestad, R., 2014. Aberration-corrected HAADF-STEM investigations of precipitate structures in Al–Mg–Si alloys with low Cu additions. Philos. Mag. 94, 520–531.

Shanthala, K., Sreenivasa, T.N., 2016. Review on electromagnetic welding of dissimilar materials. Front. Mech. Eng. 11, 363–373.

Shribman, V., 2007. Magnetic pulse welding of automotive HVAC parts. Rapp. Tech. Pulsar Ltd 8, 41–42.

Shribman, V., 2008. Magnetic pulse welding for dissimilar and similar materials, in: 3rd International Conference on High Speed Forming. Institut für Umformtechnik-Technische Universität Dortmund, 13–22.

Sun, L., Muszka, K., Wynne, B.P., Palmiere, E.J., 2011. The effect of strain path reversal on high-angle boundary formation by grain subdivision in a model austenitic steel. Scr. Mater. 64, 280–283.

Uhlmann, E., Ziefle, A., 2010. Modelling pulse magnetic welding processes–an empirical approach, in: 4th International Conference on High Speed Forming, Columbus, Ohio, USA. pp. 108–116.

Weddeling, C., Gies, S., Nellesen, J., Kwiatkowski, L., Tillmann, W., Tekkaya, A.E., 2012. Influencing Factors on the Strength of Electromagnetically Produced Form-Fit Joints using Knurled Surfaces, in: Proceedings of the 5th International Conference on High

Speed Forming–ICHSF2012. 243–254.

Wu, X., Tao, N., Hong, Y., Xu, B., Lu, J., Lu, K., 2002. Microstructure and evolution of mechanically-induced ultrafine grain in surface layer of AL-alloy subjected to USSP. Acta Mater. 50, 2075–2084.

Yang, Y., Luo, S., Hu, H., Tang, T., Zhang, Q., 2016. Diffusive transformation at high strain rate: On instantaneous dissolution of precipitates in aluminum alloy during adiabatic shear deformation. J. Mater. Res. 31, 1220–1228.

Ye, T., Wu, Y., Liu, A., Xu, C., Li, L., 2019. Mechanical property and microstructure evolution of aged 6063 aluminum alloy under high strain rate deformation. Vacuum 159, 37–44.

Zhang, Y., Babu, S.S., Daehn, G.S., 2010. Interfacial ultrafine-grained structures on aluminum alloy 6061 joint and copper alloy 110 joint fabricated by magnetic pulse welding. J. Mater. Sci. 45, 4645–4651.

Zhilyaev, A.P., Swaminathan, S., Gimazov, A.A., McNelley, T.R., Langdon, T.G., 2008. An evaluation of microstructure and microhardness in copper subjected to ultra-high strains. J. Mater. Sci. 43, 7451–7456.

Zurob, H.S., Hutchinson, C.R., Brechet, Y., Purdy, G., 2002. Modeling recrystallization of microalloyed austenite: effect of coupling recovery, precipitation and recrystallization. Acta Mater. 50, 3077–3094.